

LA-UR-17-20097 (Accepted Manuscript)

# Effects of electric field methods on modeling the midlatitude ionospheric electrodynamics and inner magnetosphere dynamics

Yu, Yiqun  
Jordanova, Vania Koleva  
Ridley, Aaron  
Toth, Gabor  
Heelis, Roderick

Provided by the author(s) and the Los Alamos National Laboratory (2017-09-26).

**To be published in:** Journal of Geophysical Research: Space Physics

**DOI to publisher's version:** 10.1002/2016JA023850

**Permalink to record:** <http://permalink.lanl.gov/object/view?what=info:lanl-repo/lareport/LA-UR-17-20097>

**Disclaimer:**

Approved for public release. Los Alamos National Laboratory, an affirmative action/equal opportunity employer, is operated by the Los Alamos National Security, LLC for the National Nuclear Security Administration of the U.S. Department of Energy under contract DE-AC52-06NA25396. Los Alamos National Laboratory strongly supports academic freedom and a researcher's right to publish; as an institution, however, the Laboratory does not endorse the viewpoint of a publication or guarantee its technical correctness.

<sup>1</sup> **Effects of electric field methods on modeling the  
2 mid-latitude ionospheric electrodynamics and inner  
3 magnetosphere dynamics**

Yiqun Yu<sup>1</sup>, Vania K. Jordanova<sup>2</sup>, Aaron J. Ridley<sup>3</sup>, Gabor Toth<sup>3</sup>, Roderick  
Heelis<sup>4</sup>

<sup>4</sup> <sup>1</sup> School of Space and Environment, Beihang University, Beijing, China

<sup>5</sup> <sup>2</sup> Space Science and Application, Los Alamos National Laboratory, Los  
<sup>6</sup> Alamos, New Mexico, USA

<sup>7</sup> <sup>3</sup> Department of Climate and Space Sciences, University of Michigan, Ann  
<sup>8</sup> Arbor, Michigan, USA

<sup>9</sup> <sup>4</sup> Department of Physics, University of Texas at Dallas, Dallas, Texas, USA

---

Corresponding author: Y. Yu, School of Space and Environment, Beihang University, Beijing,

China. (yiqunyu17@gmail.com)

**10 Abstract.** We report a self-consistent electric field coupling between the  
11 mid-latitude ionospheric electrodynamics and inner magnetosphere dynam-  
12 ics represented in a kinetic ring current model. This implementation in the  
13 model features another self-consistency in addition to its already existing self-  
14 consistent magnetic field coupling with plasma. The model is therefore named  
15 as Ring current-Atmosphere interaction Model with Self-Consistent magnetic  
16 (B) and electric (E) fields, or RAM-SCB-E. With this new model, we explore,  
17 by comparing with previously employed empirical Weimer potential, the im-  
18 pact of using self-consistent electric fields on the modeling of storm-time global  
19 electric potential distribution, plasma sheet particle injection, and the sub-  
20 auroral polarization streams (SAPS) which heavily rely on the coupled in-  
21 terplay between the inner magnetosphere and mid-latitude ionosphere. We  
22 find the following phenomena in the self-consistent model: (1) the spatially  
23 localized enhancement of electric field is produced within  $2.5 < L < 4$  during  
24 geomagnetic active time in the dusk-premidnight sector, with a similar dy-  
25 namic penetration as found in statistical observations. (2) The electric po-  
26 tential contours show more substantial skewing towards the post-midnight  
27 than the Weimer potential, suggesting the resistance on the particles from  
28 directly injecting towards the low-L region. (3) The proton flux indeed in-  
29 dicates that the plasmashell inner boundary at the dusk-premidnight sec-  
30 tor is located further away from the Earth than in the Weimer potential, and  
31 a ‘tongue’ of low energy protons extends eastward towards the dawn, lead-  
32 ing to the Harang reversal. (4) SAPS are reproduced in the subauroral re-

<sup>33</sup> gion and their magnitude and latitudinal width are in reasonable agreement  
<sup>34</sup> with data.

<sup>35</sup> 1

## 1. Introduction

36 The electric field has been long considered as a crucial element in understanding the  
37 inner magnetosphere-ionosphere coupled system, owing to its important role in governing  
38 a rich variety of dynamics in the system. In the ionosphere, the electric potential pattern  
39 typically shows two convection cells, which correspond to dawn-to-dusk convection elec-  
40 tric field over the polar cap and poleward electric field at lower latitudes. This pattern  
41 can become complex during geomagnetic disturbed conditions, including the formation  
42 of a “potential tongue” extending from premidnight to early morning sector, and an en-  
43 hancement of a penetration electric field below the Region 2 current system when the  
44 current is unable to fully shield the potential from lower latitudes. It is these additions  
45 that complicate the entire coupling processes. For instance, the “tongue” usually is asso-  
46 ciated with a flow reversal, namely the Harang reversal [Harang, 1946], where field-aligned  
47 currents (FACs) of opposite directions are overlap in the local time highly associated with  
48 substorm onset [e.g., Zou *et al.*, 2009; Gkioulidou *et al.*, 2009]. The penetration electric  
49 field can lead to phenomena such as ionospheric scintillation [Kelley and Heelis, 1989]  
50 and plasmaspheric bite-outs [Horwitz, 1987]. Its enhancement near the dusk terminator  
51 also gives rise to increased ion drift in the ionosphere, termed subauroral polarization  
52 streams (SAPS) [Foster and Burke, 2002], which are closely affiliated with ring currents,  
53 FACs, electric/magnetic fields, and hot plasma dynamics in the inner magnetosphere [e.g.,  
54 Ebihara *et al.*, 2009; Wang *et al.*, 2014; Yu *et al.*, 2015].

55 Besides the influence on the ionospheric electrodynamics, the electric field is also a  
56 primary determinant for inner magnetospheric dynamics. When the inner magnetosphere

57 can be assumed to be free of parallel potential drop, it is reasonable to approximate the  
 58 potential representing the electric field in the magnetosphere as the same as the ionospheric  
 59 potential. The convection electric field is one major element in regulating the transport  
 60 of charged particles from the tail plasmashell towards the Earth inner region [Cao *et al.*,  
 61 2011; Zhang *et al.*, 2015], providing a source population to the ring current and radiation  
 62 belts. With the combined effect of magnetic gradient and curvature, charged particles  
 63 drift separately eastward and westward around the Earth, with the hot ring current ions  
 64 (westward drifting) carrying most of the energy content of the inner magnetosphere [Daglis  
 65 *et al.*, 1999; Daglis and Kozyra, 2002; Jordanova *et al.*, 2012]. The same electric field also  
 66 participates in the erosion of cold dense plasmaspheric particles and the formation of a  
 67 drainage plume during geomagnetic active time [e.g., Chappell *et al.*, 1970; Liu *et al.*,  
 68 2015].

69 As described above, the electric potential along magnetic field lines acts as a bridge  
 70 coupling the magnetosphere-ionosphere system. Therefore it is important to understand  
 71 not only the morphology of the electric fields but also its effects on various physical  
 72 processes in the inner magnetosphere and mid-latitude ionosphere. While observations of  
 73 the global electric field pattern are still limited due to the limitation in the coverage of  
 74 satellites in the near-Earth space, an alternative effective approach is through numerical  
 75 tools. In a height-integrated ionospheric electrodynamics model, the electric field pattern  
 76 is usually derived from a Poisson equation at the ionospheric altitude (e.g.,  $\sim 100$  km)  
 77 given two major quantities  $J_{||}$  and  $\Sigma$ :

$$\nabla \cdot (\Sigma \cdot \nabla \Phi) = -J_{||} \sin I \quad (1)$$

78 where  $J_{\parallel}$  is the FACs into and out of the ionosphere,  $\Sigma$  is the tensor of height-integrated  
79 ionospheric conductance, including both Hall and Pedersen conductances, and  $I$  is the  
80 inclination angle of the magnetic field in the ionosphere. This equation demonstrates  
81 that FACs and conductance play key roles in controlling the ionospheric electric poten-  
82 tial/field. Although these two factors are specified at the ionosphere altitude, they are  
83 mostly determined by the magnetospheric dynamics, particularly for the Region 2 FACs  
84 [Cao *et al.*, 2008, 2010] and the mid-latitude auroral conductance. The Region 2 FACs  
85 in and out of the ionosphere are diverted from the partial ring current formed during  
86 storm main phase [Vasyliunas, 1970]. The auroral conductance is mainly caused by keV  
87 electron precipitation that is scattered into the loss cone via wave particle interactions in  
88 the magnetosphere [Horne *et al.*, 2003; Ni *et al.*, 2008], namely diffuse precipitation, or  
89 accelerated down to the upper atmosphere [Newell *et al.*, 2009], namely discrete precipita-  
90 tion. Therefore, the ring current evolution and plasma wave excitation are two principal  
91 regulators of the Region-2 FACs and auroral conductance. Consequently, the electric field  
92 can be generated self-consistently knowing the ring current particle distributions, which  
93 in turn feed back to the magnetospheric plasma drift, resulting in particle distributions  
94 that are used to determine the properties of plasma waves.

95 These relationships reveal a nonlinear feedback loop in the system and also complicate  
96 the understanding of underlying physical processes. It is a challenge for first-principle  
97 modeling studies to comprehensively and self-consistently include all the coupling pro-  
98 cesses and missing physics or inconsistent cause-effect physics in the model may introduce  
99 substantial bias. In the past decades, efforts have been extensively made to improve  
100 modeling skills, not only for a better understanding of the fundamental physics, but also

101 for a more accurate, promising predictive capability of the geospace system. One pivotal  
102 task in previous modeling efforts is to specify a realistic auroral conductance pattern be-  
103 cause of its critical role in determining the electric field. One such specification relates  
104 the auroral conductance with FACs [e.g., *Ridley and Liemohn*, 2002; *Ridley et al.*, 2004;  
105 *Liemohn et al.*, 2004, 2005; *Ebihara et al.*, 2004; *Ilie et al.*, 2012; *Yu et al.*, 2015]. The  
106 relation was statistically derived from thousands of maps of the ionospheric Hall and  
107 Pedersen conductance and FACs generated by the assimilative mapping of ionospheric  
108 electrodynamics (AMIE) technique [*Richmond and Kamide*, 1988], described in *Ridley*  
109 *et al.* [2004]. It simplifies the way of prescribing the conductance and bypasses the pitfalls  
110 in embracing some direct physical processes such as diffuse auroral precipitation. While  
111 discrete auroral precipitation may be carried by FACs, diffuse precipitation caused by the  
112 wave scattering process in the magnetosphere cannot be represented by FACs. Studies  
113 also found that diffuse auroral precipitation contributes more than discrete precipitation  
114 to the energy flux deposited into the ionosphere. Another inclusive specification of auro-  
115 ral conductance in the inner magnetosphere models uses an empirical conductance model  
116 [e.g., *Hardy et al.*, 1987; *Galand and Richmond*, 2001; *Robinson et al.*, 1987] that calcu-  
117 lates conductance based on precipitation flux and energy (independent on FACs) [e.g.,  
118 *Fok et al.*, 2001; *Toffoletto et al.*, 2003; *Khazanov et al.*, 2003; *Chen et al.*, 2015a, b; *Yu*  
119 *et al.*, 2016]. In most of these studies, the precipitation flux is estimated from the loss  
120 cone particle flux, which is scattered from wave particle interactions in the inner magneto-  
121 sphere. The scattering process is crudely represented by simply applying loss rates to the  
122 particles. Such rates are called lifetimes. Determining the lifetimes of charged particles at  
123 various energies is also one popular research topic in the inner magnetosphere community

<sub>124</sub> [e.g., *Albert and Shprits*, 2009; *Artemyev et al.*, 2013; *Li et al.*, 2013] as it is essential for  
<sub>125</sub> understanding the dynamics of energetic particles in both ring current and radiation belt.  
<sub>126</sub> Recently, *Yu et al.* [2016] applied pitch angle diffusion coefficients, rather than lifetimes,  
<sub>127</sub> to account for the wave-particle scattering processes and showed significant improvement  
<sub>128</sub> over using a lifetime method in reproducing the measured spatial and temporal evolution  
<sub>129</sub> of ionospheric electron precipitation. This new capability leads to a more realistic auroral  
<sub>130</sub> precipitation pattern, and is deemed to be more suitable for a physical representation of  
<sub>131</sub> auroral conductance and for studying subauroral physics.

<sub>132</sub> It should be noted that *Yu et al.* [2016] implemented such a precipitation module within  
<sub>133</sub> a fully coupled MHD-kinetic framework, not in a stand-alone kinetic ring current model.  
<sub>134</sub> Within that framework, the ionospheric electric potential is computed from the Poisson  
<sub>135</sub> equation with FACs calculated in the MHD model and auroral conductance determined  
<sub>136</sub> by the electron precipitation from the ring current model. It is known that the MHD  
<sub>137</sub> code coupled with a kinetic ring current model produces stronger distortion of the global  
<sub>138</sub> magnetic field owing to the inclusion of kinetic physics in the inner magnetosphere, and the  
<sub>139</sub> Region-2 FACs at mid-latitude, deviation from the ring current, is significantly improved  
<sub>140</sub> over pure-MHD results [*De Zeeuw et al.*, 2004]. But the Region-2 FACs are still weaker  
<sub>141</sub> and more diffuse than observations [*Zaharia et al.*, 2006; *Yu et al.*, 2016], mainly because  
<sub>142</sub> the ring current pressure in the MHD model is only nudged towards but does not exactly  
<sub>143</sub> match the pressure in the kinetic ring current model. One consequence of a weaker Region-  
<sub>144</sub> 2 FAC is that the lower-latitude electric field may be undershielded [*Yu et al.*, 2016] and  
<sub>145</sub> the inner boundary of plasmashell resides closer to the Earth. Also the MHD grid stops  
<sub>146</sub> at  $\sim 2.5 R_e$ , so low-latitude currents are not well captured in the MHD code. Therefore, in

<sup>147</sup> order to achieve a more realistic, fully self-consistent closure of the ring current-ionosphere  
<sup>148</sup> coupled system, the Region-2 FACs should be simultaneously determined from the ring  
<sup>149</sup> current dynamics rather than from MHD fields.

<sup>150</sup> In this study, we utilize the newly developed physics-based and more realistic electron  
<sup>151</sup> precipitation module in *Yu et al.* [2016] and the Region-2 FACs calculated from a stand-  
<sup>152</sup> alone ring current model RAM-SCB (i.e., Ring current Atmosphere interaction Model  
<sup>153</sup> with Self-Consistent magnetic field (B)) [*Jordanova et al.*, 2006, 2010; *Zaharia et al.*,  
<sup>154</sup> 2006, 2010] to self-consistently yield the electric field. We further investigate the global  
<sup>155</sup> electric potential pattern, plasmashell particle injection, and more importantly the SAPS,  
<sup>156</sup> a physical process that is closely associated with electron precipitation and Region-2 FACs  
<sup>157</sup> [*Foster and Burke*, 2002]. The ring current model RAM-SCB possesses a self-consistent  
<sup>158</sup> magnetic field, and computes differential particle distributions within a prescribed electric  
<sup>159</sup> field that is usually updated from empirical electric field/potential models [e.g., *Volland*,  
<sup>160</sup> 1973; *Stern*, 1975; *Weimer*, 2001; *Weimer*, 2005]. The problem with these empirical  
<sup>161</sup> electric field models is that they are not self-consistent with the first-principle calculated  
<sup>162</sup> hot plasma dynamics. Therefore, in this study, the ring current model will be updated to  
<sup>163</sup> calculate the electric field self-consistently, resulting in an even more self-consistent and  
<sup>164</sup> comprehensive treatment of the plasma and fields.

## 2. Methodology

<sup>165</sup> In this section, the kinetic ring current model RAM-SCB-E is presented in detail and  
<sup>166</sup> the magnetic storm event under investigation is also described.

## 2.1. Model description

167 In order to best represent the physics in the inner magnetosphere-ionosphere system,  
 168 the kinetic ring current model is solved with electric/magnetic fields self-consistently de-  
 169 termined based on the solution of the ring current phase space distribution. Figure 1 illus-  
 170 trates how the coupling physics is fulfilled numerically. First, the Ring current-Atmosphere  
 171 interaction model (RAM) [Jordanova *et al.*, 2006, 2010] solves the Fokker-Planck equations  
 172 for both ring current ions and electrons to yield their distribution functions  $Q_l(R, \phi, E, \alpha)$ :

$$\begin{aligned} \frac{\partial Q_l}{\partial t} + \frac{1}{R_o^2} \frac{\partial}{\partial R_o} (R_o^2 < \frac{dR_o}{dt} > Q_l) + \frac{\partial}{\partial \phi} (< \frac{d\phi}{dt} > Q_l) \\ + \frac{1}{\gamma p} \frac{\partial}{\partial E} (\gamma p < \frac{dE}{dt} > Q_l) + \frac{1}{h\mu_o} \frac{\partial}{\partial \mu_o} (h\mu_o < \frac{d\mu_o}{dt} > Q_l) \\ = < (\frac{\partial Q_l}{\partial t})_{loss} > \end{aligned} \quad (2)$$

173 where  $Q_l$  is a function of radial distance  $R$  from 2 to  $6.5 R_e$  with spatial resolution of  
 174  $0.25 R_e$ , geomagnetic east longitude  $\phi$  with resolution of  $15^\circ$ , energy  $E$  between 0.15 to  
 175 400 keV, and pitch angle  $\alpha$  from 0 to  $90^\circ$ . The subscription  $l$  represents the species,  
 176 the bracket  $<>$  represents bounce averaging, the subscript index  $o$  denotes the magnetic  
 177 equatorial plane,  $p$  is the relativistic momentum of the particle,  $\gamma$  is the Lorentz factor,  
 178 and  $h$  is defined by:

$$h(\mu_o) = \frac{1}{2R_0} \int_{s_m}^{s'_m} \frac{ds}{\sqrt{(1 - B(s)/B_m)}} \quad (3)$$

179 which is proportional to the bounce period. Here,  $B_m$  is the magnetic field at the mirror  
 180 point,  $ds$  is a distance interval along the field line, and  $R_0$  is the magnetic equatorial  
 181 distance of the field line.

182 The loss terms on the right hand side of Equation (2) represent several physical pro-  
 183 cesses, including charge exchange with geocoronal hydrogen for ring current ions, atmo-  
 184 spheric collisional loss for both electrons and ions, and wave induced scattering loss for  
 185 electrons. Such scattering loss of keV electrons is induced by whistler mode chorus and  
 186 hiss waves outside and inside the plasmapause respectively, resulting in electron precipi-  
 187 tation. This process is numerically described by a diffusion equation of the distribution  
 188 function, using pitch angle diffusion coefficients obtained from statistical satellite obser-  
 189 vations [*Glauert and Horne, 2005; Horne et al., 2013; Glauert et al., 2014; Albert, 2005*].  
 190 These coefficients take into account the effect of both whistler mode chorus and hiss waves  
 191 on scattering electrons from tens of eV to hundreds of keV into the loss cone. The differen-  
 192 tial electron flux within loss cones is subsequently integrated to produce the precipitation  
 193 energy flux  $F_E$  (details can be found in *Yu et al. [2016]* regarding the wave-induced loss  
 194 and the conversion of particle distributions at the equator to the total precipitation flux  
 195 in the ionosphere) .

196 RAM is coupled to a 3D magnetic field equilibrium code that computes the magnetic  
 197 field [*Zaharia et al., 2004*] from the anisotropic plasma pressure provided by RAM. The  
 198 resulting magnetic field in turn is used in determining the transport of charged particles  
 199 and changes in their distributions [*Jordanova et al., 2006; Zaharia et al., 2006*]. This  
 200 coupling is updated every 5 minutes.

201 In addition to this existing magnetic field self-consistency in the model, the electric  
 202 field is also self-consistently determined at the ionospheric altitude  $\sim 100\text{km}$  based on the  
 203 Poisson Equation (1). As the equatorial computational domain of RAM is confined within  
 204 2.0-6.5  $R_e$ , the outermost closed magnetic field lines often find their footprints at magnetic  
 205 latitudes between 70° and 60°, highly depending on the magnetospheric configuration. So  
 206 while solving the electric potential in the ionosphere, the high-latitude boundary is time-  
 207 varying. But the low-latitude boundary is fixed at 30°. The high-latitude boundary  
 208 condition is enforced by the potential calculated from the Weimer 2K model [Weimer,  
 209 2001], driven by solar wind/interplanetary magnetic field (IMF) conditions and AL index,  
 210 and the low-latitude boundary condition of potential is zero.

211 To solve the potential with Equation 1 that takes inputs of FACs and conductance,  
 212 FACs are firstly obtained from the Vasyliunas equation [Vasyliunas, 1970] that relates  
 213 the field-aligned current density  $J_{\parallel}$  to the magnetic equatorial hot plasma conditions,  
 214 specifically the gradient in the plasma pressure and magnetic field [Zaharia *et al.*, 2010]:

$$\mathbf{B} \cdot \nabla \left( \frac{J_{\parallel}}{B} \right) = \frac{2\mathbf{B} \cdot (\nabla \cdot \mathbf{P} \times \boldsymbol{\kappa})}{B^2}. \quad (4)$$

215 where  $\boldsymbol{\kappa} = (\mathbf{b} \cdot \nabla \mathbf{b})$  is the field line curvature. The above equation is derived from the  
 216 charge neutrality  $\nabla \cdot \mathbf{J} = 0$ . To obtain FACs at the ionospheric altitude, we integrate the  
 217 above equation along magnetic field lines from the magnetic equator to the ionosphere.

218 Then, the conductance is determined from a combination of dayside conductance asso-  
 219 ciated with solar radiation, and auroral conductance contributed by diffusive and discrete  
 220 electron precipitation. The dayside solar EUV induced conductance is obtained by an

<sup>221</sup> empirical function based on the solar zenith angle and the F10.7 index [Moen and Brekke,  
<sup>222</sup> 1993]. The auroral conductance is calculated according to the empirical Robinson relation  
<sup>223</sup> [Robinson *et al.*, 1987] using precipitation energy flux  $F_E$  obtained from RAM as men-  
<sup>224</sup> tioned above for the diffusive aurora and using the FACs for the discrete aurora (Details  
<sup>225</sup> can be found in Yu *et al.* [2016]).

<sup>226</sup> Hence, with the electric potential solved from FACs and conductance both determined  
<sup>227</sup> by the hot plasma physics, this well coupled scheme (Figure 1) is termed RAM-SCB-E,  
<sup>228</sup> that is, Ring current-Atmosphere interaction Model with Self-Consistent magnetic (B)  
<sup>229</sup> and electric (E) fields.

## 2.2. Event description and model setup

<sup>230</sup> We simulate a magnetic storm event that occurred on August 31, 2005 with RAM-  
<sup>231</sup> SCB-E. Figure 2 shows that during this event, the IMF turns southward around 12:00  
<sup>232</sup> UT accompanied by a large solar wind density that is sustained above  $20 \text{ cm}^{-3}$  for a few  
<sup>233</sup> hours. The magnetic field remains southward for nearly 10 hours, but the solar wind speed  
<sup>234</sup> stays around 400 km/s. A minimum SYM-H index is recorded to be -120 nT at 19:00  
<sup>235</sup> UT before it gradually recovers. The AL index frequently hits 1000 nT. Some of these  
<sup>236</sup> solar wind and geomagnetic conditions are used to determine the time-varying Weimer  
<sup>237</sup> electric potential at the high-latitude boundary in the model. The plasma sheet boundary  
<sup>238</sup> condition at  $6.5 R_e$  is taken from LANL/SOPA and MPA satellites that measure electron  
<sup>239</sup> and ion fluxes. The fluxes are then interpolated into all local times and energy grids within  
<sup>240</sup> the model, and are further decoupled into proton, helium and oxygen ions according to  
<sup>241</sup> Young *et al.* [1982]'s statistical results on the ratios of these ion species. Figure 3 shows  
<sup>242</sup> such a boundary condition at  $\text{MLT} = 0$  as an example. The low-energy proton flux is

243 consistently high during the entire event, but the high-energy flux (above 30 keV) shows  
 244 drastic injections after 12:00 UT. On the other hand, injection occurs at 10:00 UT for  
 245 low-energy electrons, and similarly high-energy electrons experience continual injections  
 246 in the storm main phase. These plasmashell injections provide important sources to the  
 247 ring current, as will be demonstrated in the simulation result. The magnetic field at the  
 248 outer most shell of the 3D magnetic field code is specified by the Tsyganenko magnetic  
 249 field model [Tsyganenko, 1989] parameterized by the Kp index.

### 3. Results

250 Two simulations are conducted for the storm event: one uses a self-consistent electric  
 251 field as described above, and the other one uses a prescribed electric potential model (i.e.,  
 252 [Weimer, 2001]) in governing the ring current particle transport. The latter, based on  
 253 statistical observations, cannot represent the feedback effects of the changes in the hot  
 254 populations on the ionospheric electrodynamics in this particular simulation. That is,  
 255 the part inside the dashed rectangle in Figure 1 is not represented in the simulation. By  
 256 comparing these two types of simulation, we intend to address the following questions:  
 257 How different is the self-consistent electric field from empirically obtained representation?  
 258 What are the influences on inner magnetosphere drift physics? What are the influences  
 259 on ionospheric electrodynamics?

#### 3.1. Effect on the inner magnetospheric dynamics

260 Figure 4 illustrates electric potential contours and dawn-to-dusk convection electric  
 261 fields ( $E_y$ ) mapped from the ionospheric altitude where the potential is solved with Equa-  
 262 tion (1) during the storm main phase for both simulations. Two main features are distinc-

263 tive: (1) The potential contour lines from the self-consistent solver show stronger skewing  
 264 in the dusk-to-post-midnight sector than the Weimer potential contours; (2) The Weimer  
 265 model shows a much stronger dawn-to-dusk electric field ( $E_y$ ) in the dusk sector than in  
 266 the self-consistent case. While the potential contour skewing may suggest an effect from  
 267 the transport of energetic particles, the localized electric field enhancement indicates the  
 268 degree of penetration of the convection.

269 It is also known that the potential contour skewing is associated with inner magne-  
 270 tosphere shielding that prevents the convection electric field in the outer magnetosphere  
 271 from penetrating into the inner region. The above difference in the potential patterns sug-  
 272 gests that the Weimer potential is less shielded than the self-consistent potential, because  
 273 the latter experiences a weaker penetration field. To demonstrate the penetration and  
 274 shielding effects during the entire storm event, Figure 5 shows the dawn-to-dusk compo-  
 275 nent of convection electric field ( $E_y$ ) at MLT=20, as a function of radial distance and UT  
 276 time. Localized enhancements of penetration electric field are evident in both cases but  
 277 with remarkable differences. The self-consistent solver displays gradual migration of the  
 278 peak of the penetration electric field, with the electric field well shielded in the pre-storm  
 279 time at 12:00 UT, and then penetrating from  $L = 4.5$  to  $3.0$  during storm main phase  
 280 until retreating back to  $L = 4$  in the early recovery phase. Such a process precisely implies  
 281 the competition between the establishment of Region-2 FACs, ionospheric currents, and  
 282 changes in the convection strength. While changes in the convection that respond with a  
 283 longer time scale than the currents may be effectively shielded, sudden transitions like the  
 284 IMF southward turning can lead to a rapid increase in the polar cap potential, causing  
 285 large penetration of the convection electric field. But meanwhile the formation and en-

286 hancement of ring current, FACs, and ionospheric currents create a shielding electric field  
287 in the ionosphere (Region-2 FACs are connected with dusk-to-dawn Pedersen current in  
288 the nightside sector), opposing the penetration and resulting in a “residual” dawn-to-dusk  
289 convection electric field in the undershielded situation.

290 In contrast, with a Weimer potential model, since the FACs and ionospheric currents  
291 do not respond self-consistently to oppose the dawn-to-dusk convection electric field, the  
292 penetration electric field is much greater and extends to lower L shells, even during pre-  
293 storm time. The peak of the penetration electric field is located around L=2.5 or even  
294 closer, regardless of the storm phase. The gradual inward motion of the penetration along  
295 with the development of the ring current is not present, indicating a non self-consistent  
296 response between the ring current, FACs, ionospheric current, and the prescribed electric  
297 field.

298 The radially localized enhancement of the penetration electric field has been statistically  
299 studied using satellite observations [e.g., *Rowland and Wygant*, 1998; *Nishimura et al.*,  
300 2006, 2007; *Matsui et al.*, 2004, 2013] for different geomagnetic activity levels. The obser-  
301 vational studies show that the dawn-to-dusk electric field in the dusk sector of the inner  
302 magnetosphere usually increases with radial distance under quiet and less disturbed condi-  
303 tions, but a localized peak of the electric field appears around L = 3-4 for disturbed time,  
304 and moves outward during storm recovery phase. In agreement with the observational  
305 results, our simulation with a self-consistent electric field produces a similar dynamic elec-  
306 tric field penetration that varies with the evolution of the ring current. This approach  
307 therefore shows a more reasonable and consistent picture of the radial distribution of the  
308 dawn-to-dusk electric field.

309 To examine the effect of the potential pattern on particle transport, we next study  
 310 the particle injections from the outer boundary. When particles travel through the in-  
 311 ner magnetosphere, they experience various electric and magnetic drifts induced by the  
 312 perpendicular electric field and the gradient and curvature of the magnetic field. The  
 313 electric potential contours represent the drift trajectory of zero-energy particles, while  
 314 higher-energy particles are more subject to magnetic gradient and curvature drift. From  
 315 the electric potential pattern across midnight in Figure 4, we expect to see a diverted  
 316 flow of low-energy protons in the simulation with a self-consistent electric field and direct  
 317 injection in the simulation with the Weimer model. Indeed, Figure 6 illustrates that under  
 318 the influence of a self-consistent electric field (Figure 6 (a) top panel), protons at  $E = 9.3$   
 319 keV in the dusk-premidnight sector are convected inward from the outer boundary and  
 320 their flux significantly drops near  $L = 2.5$ . In contrast, these low-energy protons maintain  
 321 high-level flux down to  $L = 2$  and eventually get lost from the inner boundary when the  
 322 Weimer electric field is utilized (Figure 6 (b) top panel). At higher energies, the proton  
 323 injections from the outer boundary down to the inner region behave similarly in both  
 324 cases, so do the electrons in the early morning sector (Figure 6 (c, d)). This similarity  
 325 in the electron dynamics is probably attributed to the similar electric potential contours  
 326 and magnetic field configuration in the dawn sector.

327 Although high-energy protons above 30 keV are the dominant contributor to the ring  
 328 current energy and carry most of the energy content of the inner magnetosphere, low-  
 329 energy ions are of particular importance to the pre-midnight electrodynamics, especially  
 330 in the Harang reversal commonly detected in the ionosphere. *Gkioulidou et al.* [2009]  
 331 conducted detailed analysis of the Rice Convection Model (RCM) simulation and found

332 that a pair of FACs with opposite polarity overlaps near the same midnight local time  
333 across different latitudes is necessary for the formation of the Harang reversal. Such a  
334 pair of FACs (downward and upward) is found to be associated with low energy ions  
335 penetrating closer to the Earth towards the dawn side and high energy ions that are  
336 further away from the Earth. In this study, the simulation with a self-consistent electric  
337 field presents a “tongue” of 9.3 keV protons extending across midnight towards dawn in  
338 the low L-shell region, as shown in Figure 7, but limited extension is developed in the  
339 Weimer case. On the other hand, the Weimer model does not allow high-energy protons to  
340 extend towards the dawn or penetrate as deeply. Such an extension of low energy protons  
341 in wider MLT coverage, as concluded in *Gkioulidou et al.* [2009], is highly related to the  
342 downward FACs into the ionosphere, which can control the ionospheric electrodynamics  
343 to be discussed in the next section. In contrast, the Weimer electric potential does not  
344 interact with the real-time FACs originating from the inner magnetosphere.

### 3.2. Effect on the ionospheric electrodynamics

345 Figure 8 (a) displays the FACs at the ionospheric altitudes calculated from the ring  
346 current. As expected, downward FACs in the dusk side extend across local midnight to-  
347 wards the dawn side, equatorward of the upward FACs. An MLT-overlap region is formed  
348 near midnight, allowing for the formation of the Harang reversal [*Gkioulidou et al.*, 2009].  
349 Figure 8 (b) presents the conductance contributed from a combination of solar irradiance  
350 and auroral precipitation originating from the wave-induced pitch angle scattering of ring  
351 current electrons. An enhanced auroral conductance is evident around 60° in the pre-  
352 midnight to the dawn sector as the chorus waves responsible for the electron scattering  
353 are mostly active in that region. From FACs and conductance, the self-consistent electric

354 potential is generated (Figure 8 (c)). A “tongue” of the negative potential cell (potential  
355 well) in the dusk side stretches into early morning at low latitudes, representing the Ha-  
356 rang reversal. The westward return flows in the reversal at lower latitudes are located on  
357 top of the collapsed potential contour lines (i.e., a large electric field) where conductance  
358 is low, resulting in enhanced flow speed, or SAPS, shown in Figure 8 (d). The speed  
359 exceeds 1000 m/s around latitude of 55° in the dusk-to-premidnight sector, a typical loca-  
360 tion reported from observations. By contrast, the Weimer potential pattern (Figure 8 (e,  
361 f) has neither extension of the negative cell nor tightly collapsed contour lines, meaning  
362 that SAPS are not prominent.

363 To verify that the flow in the self-consistent simulation is indeed SAPS, the subauroral  
364 region is first identified. It is defined as that region located below the equatorward edge  
365 of auroral precipitation. Figure 9 (d) shows the auroral precipitation energy flux at MLT  
366 = 21 as a function of latitude. A rapid drop of the precipitation energy flux marks the  
367 equatorward edge of the auroral boundary, denoted by the vertical dashed line. In the  
368 subauroral region, the precipitation flux is about three orders of magnitude lower, and the  
369 conductance falls to 0.5 mhos. The downward Region-2 FACs flow into this subauroral  
370 region, and a strong poleward electric field is produced in order to drive the horizontal  
371 Pedersen current that connects to the upward Region-1 FACs at higher latitudes. This  
372 leads to an enhancement of westward flows in the subauroral region, namely SAPS at ~54°  
373 latitude. As a flow speed above 500 m/s in the subauroral region is commonly referred as  
374 SAPS, it is found that SAPS occur in the region equatorward of the enhanced Pedersen  
375 conductance and concurrent with both Region-1 and -2 FACs. The SAPS peak is located  
376 between the peaks of Region-1 and Region-2 FACs with the Region-2 FAC well below the

<sup>377</sup> equatorward edge of the auroral boundary. These relative positions are in agreement with  
<sup>378</sup> statistical observational results reported in *Wang et al.* [2014], and reveal relationships  
<sup>379</sup> consistent with the current-generator mechanism proposed in *Anderson et al.* [1991, 2001].

<sup>380</sup> Figure 10 shows simulation results extracted along two consecutive DMSP trajectories  
<sup>381</sup> in the subauroral region in the dusk-premidnight sector when the satellite flew across  
<sup>382</sup> the polar cap region approximately from 21:00 MLT towards 09:00 MLT in the northern  
<sup>383</sup> hemisphere. Due to the cutoff at the high-latitude boundary, the model only shows results  
<sup>384</sup> at mid-latitudes which, however, sufficiently describe the subauroral dynamics. Along the  
<sup>385</sup> first orbit, the spacecraft first measures a negative sunward flow, peaking around the  
<sup>386</sup> latitude of 52°, and decreases with increasing latitude. It then detects an increase of flow  
<sup>387</sup> speed again above 60°, which is the auroral zone flow at higher latitude. Such a trend is  
<sup>388</sup> well captured by the simulation (blue line), which shows a comparable magnitude for the  
<sup>389</sup> SAPS. The observed peak of SAPS however appears at lower latitudes by 2-3° and flow  
<sup>390</sup> channel is narrower. In the second orbit, the model reproduces a comparable width of the  
<sup>391</sup> flow channel, which again misses the observed peak flow by 2-3° towards higher latitudes.

<sup>392</sup> In the bottom panels, the Pedersen conductance is compared. The Pedersen conductance  
<sup>393</sup> based on observations is computed from both electron and ion precipitation measured  
<sup>394</sup> by the DMSP spacecraft. The electron associated conductance is computed from  
<sup>395</sup> the Robinson relation [*Robinson et al.*, 1987] (black dashed line), while the ion associated  
<sup>396</sup> (mainly protons) conductance is from the Galand & Richmond relation [*Galand and*  
<sup>397</sup> *Richmond*, 2001]. Both relations take into account the precipitation energy flux and av-  
<sup>398</sup> eraged energy. It can be clearly seen during the first orbit that the proton precipitation  
<sup>399</sup> significantly contributes to the auroral conductance below the equatorward edge of the

400 electron precipitation boundary, although the second orbit shows a much smaller contribution  
401 near that region. Such a difference is attributed to the time-varying separation  
402 between the inner boundaries of the ion and electron plasmasheets. During the second  
403 orbit, the separation is not very clear, probably owing to a weaker electric potential at  
404 that time. Nevertheless, between these two inner boundaries, the ion precipitation can  
405 not be neglected given that it significantly enhances the auroral conductance near the  
406 equatorward edge of the auroral boundary. In the simulation, the conductance rapidly  
407 increases near the equatorward boundary of the observed electron auroral zone, but the  
408 magnitude is highly underestimated. This may be caused by an inadequate precipitation  
409 flux into to the ionosphere. It is possible that the statistical averaged pitch angle diffusion  
410 coefficients used to account for electron loss are not strong enough or representative in this  
411 intense storm event, or that whistler mode waves are not the only driver of diffuse electron  
412 precipitation, or that the electron energy distributions can be altered during the precipi-  
413 tation process from the magnetosphere to the ionosphere so the integrated precipitation  
414 energy flux at the ionospheric altitude is larger than that in the magnetospheric source  
415 region. It should also be noted that the ion precipitation is not yet incorporated into the  
416 model, which might be an additional cause of the underestimation. Our future study will  
417 add ion precipitation caused by magnetic field line curvature scattering and EMIC waves  
418 and further examine their relative importance in the ionospheric electrodynamics.

#### 4. Discussion

419 In the above comparisons, we noticed that although the magnitude and width of the  
420 SAPS channel produced by RAM-SCB-E are in reasonable agreement with the data, they  
421 appear at slightly higher latitudes than observed. This is probably associated with a

weaker representation of the ring current in the simulation. Figure 11 shows the simulated Dst index, calculated with the Dessler-Parker-Sckopke (DPS) relationship [Dessler and Parker, 1959; Sckopke, 1966] from the content of ring current energy. It is not as strong as the measured SYM-H index. A weaker ring current creates a more dipolar magnetic field configuration in which the footprints of the magnetic field lines lie at higher latitudes than in reality. The underestimate of ring current may be associated with the boundary conditions of plasmashell flux that were not realistically specified over all local times, because the flux at 24 local times are interpolated from three well-separated geosynchronous LANL satellites in this simulation. This may lead to underestimated plasmashell sources convecting from the tail into the inner magnetosphere, creating a ring current with smaller strength. Indeed, during the storm main phase, these three satellites are located from post-midnight to the dayside, corotating eastward, missing the important source region in the dusk-midnight sector. This means that highly-possible localized injections in that region are not captured by these satellites nor included in the simulation, which is likely the reason of underestimation. We conducted an experiment that increases the boundary flux by a factor of 1.5, and found that the ring current, as expected, is enhanced and the Dst index is closer to the observation. However, the position of Region-2 FACs flowing into the ionosphere in the subauroral region is not greatly changed, probably because the nondipolar configuration in the inner region is not significantly altered. Thus, the boundary condition does not seem to be the direct or only cause of the mismatch of the SAPS peak. It should be noted that the tail current and other induced currents on ground may also contribute to the SYM-H index during storm main phase. If that compensates the simulated Dst index, the ring current is actually not

445 significantly underestimated. Therefore, other causes should be sought for the offsetting  
446 of the position of SAPS. Nevertheless, inadequate specification of the outer boundary  
447 potential may be an improvement that requires further attention.

448 We then propose another possibility that causes the location of SAPS appearing at  
449 higher latitude. It maybe lie in the location of precipitation since the equatorward edge  
450 of the electron precipitation is closely related to the location of the SAPS peak. To cap-  
451 ture the right position of the SAPS, a better representation of the auroral precipitation is  
452 another critical element. We also notice from the data that the ion precipitation actually  
453 contributes significantly to the auroral conductance, particularly below the equatorward  
454 edge of the electron precipitation. This contributes to an additional enhancement of  
455 conductance equatorward of the electron aurora. Yet, in the simulation, not only the ion  
456 precipitation is missing, but the electron precipitation is also insufficiently included. These  
457 combined effects may contribute to the underestimation in the conductance and the devi-  
458 ation of the location of SAPS. We performed an experiment that shifts the equatorward  
459 edge of the aurora (i.e., maps the precipitation flux) towards lower latitudes by  $2^\circ$ , and  
460 found the peak of SAPS appearing at lower latitudes, consistent with the observations.  
461 Such an experiment suggests the importance of a correct location of the equatorward  
462 edge of auroral precipitation, which might be complemented by the ion precipitation.  
463 The implementation of such ion precipitation will be our next research task.

464 In revealing the SAPS features, we are aware that observations often reported that SAPS  
465 are well separated from the high-latitude auroral returning flow in the same westward  
466 direction, thus featured a “double-dip” profile in the velocity [Foster and Burke, 2002].  
467 The spatial separation is small but varies from one degree to a few degrees. In our

468 simulation, due to the limited coverage of the simulation domain, the high-latitude auroral  
469 region is not fully resolved by the model, and the high-latitude westward flow is not well  
470 produced in the storm main phase as shown in Figure 8. Nevertheless, during early storm  
471 main phase (e.g., around 13 - 14 UT) when the high-latitude boundary of the ionospheric  
472 solver is still around  $65^\circ$  in the dusk-to-premidnight sector due to less stretched magnetic  
473 field configuration, the auroral returning flow is captured above  $60^\circ$ , forming two westward  
474 flows around MLT from 19 to 22, hence consistent with observations.

475 Regarding the finite width of the SAPS channel, we expect a finer resolution of the  
476 model may sharpen the narrow-scale features. The current spatial resolution of  $0.25 R_e$   
477 in the equatorial plane corresponds to a spatial separation of  $1^\circ$  around magnetic latitude  
478 of  $60^\circ$ , and  $2.5^\circ$  separation around magnetic latitude of  $50^\circ$ . Such a model resolution  
479 may smear out small-scale fluctuations in the electric field or velocity, leading to averaged  
480 results. A finer resolution thus is in demand in the future for a better performance of  
481 resolving small-scale features.

## 5. Summary

482 This study investigated the effects of using a self-consistent treatment of electric field  
483 in the kinetic ring current model on the hot plasma dynamics and electrodynamics espe-  
484 cially in the mid-latitude ionosphere. The ring current model thus includes both electric  
485 and magnetic field self-consistency, and is named RAM-SCB-E. The new model uses  
486 a recently developed, physics-based electron precipitation module that accounts for the  
487 diffusive pitch angle scattering processes caused by whistler waves by using pitch-angle  
488 dependent diffusion coefficients. Such a module gives rise to a more realistic temporal  
489 and spatial distribution of electron precipitation [Yu *et al.*, 2016] and provides a more

realistic auroral precipitation pattern needed in specifying the ionospheric conductance in the model. While *Yu et al.* [2016] used this module in a coupled framework in which the ring current model is coupled to an MHD code, this study only treats the ring current model in a stand-alone fashion. It is a big advancement from the previous stand-alone version of the ring current model using empirical electric fields that omit the feedback effect of the hot plasma physics on the large-scale convection electric field.

Two simulations are performed using either a self-consistent electric field or the empirical Weimer potential. Significant differences are found, especially in the transport of low-energy protons and the electrodynamics that are closely associated with the coupling between the inner magnetosphere and the mid-latitude ionospheric region. It is these dynamics that play an important role in controlling the coupling processes and emphasize the necessity of modeling the system in a self-consistent manner to account for the complicated interactions within it.

When comparing these two approaches, we found the following results:

1. RAM-SCB-E produces local enhancements of penetration electric field in the dusk-premidnight sector, the peak of which gradually evolves to lower L shells as the ring current is being built up, whereas the empirical model produces a larger and more stable penetration electric field inside  $L=3$  during the entire storm event. The former is thus in better agreement with statistical results reported in *Rowland and Wygant* [1998], which showed that the spatial distribution of the local electric field enhancement in the dusk sector depends on the geomagnetic activity level.

2. The electric potential pattern in the magnetic equatorial plane shows more predominant skewing in the dusk-premidnight sector around  $L = 4$  in the self-consistent case

513 than in the empirical model case, causing more shielding from the outer region. The low-  
514 energy protons are thus transported along different paths rather than directly along the  
515 Sun-Earth direction. They are diverted azimuthally eastward, and can not reach the deep  
516 inner magnetosphere in the dusk-midnight sector as they do under the Weimer potential.  
517 For high-energy protons and electrons, no significant difference is found.

518 3. Since the low-energy protons are associated with FACs in the mid-latitude [Gkiouli-  
519 *dou et al.*, 2009], they are closely related to the mid-latitude electrodynamics, which  
520 reflects the feedback effect within the coupled system. We found that the eastward ex-  
521 tending FACs in the mid-latitudes induce the Harang reversal that is missing in the  
522 Weimer model.

523 4. Another outstanding feature in the subauroral region is that subauroral polarization  
524 streams (SAPS) are captured when using a self-consistent electric field, but are not distin-  
525 guished in the empirical model. RAM-SCB-E also verifies the popular current-generator  
526 mechanism for SAPS, which are proposed to be generated when FACs flow into the sub-  
527 auroral ionosphere where the conductance is relatively low with respect to the auroral  
528 zone.

529 Besides the above results, we realize that even more self-consistent physics is further  
530 needed in order to understand the underlying processes more precisely. In this study,  
531 albeit with the physics-based precipitation flux down to the ionospheric altitude, the cal-  
532 culation of auroral conductance still relies on the empirical Robinson formalism under  
533 an assumption of Maxwellian distribution. Removing this empirical limitation is cur-  
534 rently in progress, typically by coupling the inner magnetosphere model with an upper  
535 atmosphere model, which, given the auroral precipitation flux, determines the vertical

536 ionization profile and thus the ionospheric conductivity. This will establish a truly self-  
537 consistent mid-latitude ionospheric electrodynamics with the inner magnetosphere. Re-  
538 cently, one such effort was reported in *Huba and Sazykin* [2014]; *Huba et al.* [2017] that  
539 coupled the global ionosphere-plasmasphere model SAMI3 with the ring current model  
540 RCM and demonstrated the underlying processes within the ionosphere-plasmasphere-ring  
541 current system. These studies not only revealed the power of self-consistent modeling of  
542 fundamental physics, but also initiated the direction to more comprehensively accounting  
543 for the coupled system.

544 **Acknowledgments.** The authors thank the OMNIweb from NASA Goddard Space  
545 Flight Center for providing the solar wind/interplanetary field data and the Kyoto, Japan  
546 World Data Center System for providing the SYM-H index and AE index. The DMSP  
547 particle detectors were designed by Dave Hardy of AFRL, and the data are obtained from  
548 JHU/APL. This work was supported by the NSFC grants 41574156 and 41431071, by  
549 the Fundamental Research Funds for the Central Universities, by the Special Program for  
550 Applied Research on Super Computation of the NSFC-Guangdong Joint Fund, and by  
551 the Chinese Program for Thousands Young Talents. The work at LANL was conducted  
552 under the auspices of the U.S. Department of Energy, with partial support from the Los  
553 Alamos National Laboratory Directed Research and Development (LDRD) program under  
554 contract DE-AC52-06NA25396. Part of these simulations were performed on TianHe-2  
555 at National Supercomputer Center in Guangzhou, China. Data used in the study will be  
556 made available upon request by contacting the corresponding author.

## References

557 Albert, J., and Y. Shprits (2009), Estimates of lifetimes against pitch angle diffu-  
 558 sion, *Journal of Atmospheric and Solar-Terrestrial Physics*, 71(16), 1647 – 1652, doi:  
 559 <http://dx.doi.org/10.1016/j.jastp.2008.07.004>, toward an Integrated View of Inner Mag-  
 560 netosphere and Radiation Belts.

561 Albert, J. M. (2005), Evaluation of quasi-linear diffusion coefficients for whistler mode  
 562 waves in a plasma with arbitrary density ratio, *Journal of Geophysical Research: Space*  
 563 *Physics*, 110(A3), doi:10.1029/2004JA010844, a03218.

564 Anderson, P. C., R. A. Heelis, and W. B. Hanson (1991), The ionospheric signatures of  
 565 rapid subauroral ion drifts, *Journal of Geophysical Research: Space Physics*, 96(A4),  
 566 5785–5792, doi:10.1029/90JA02651.

567 Anderson, P. C., D. L. Carpenter, K. Tsuruda, T. Mukai, and F. J. Rich (2001), Multi-  
 568 satellite observations of rapid subauroral ion drifts (said), *jgr*, 106(A12), 29,585–29,599,  
 569 doi:10.1029/2001JA000128.

570 Artemyev, A. V., D. Mourenas, O. V. Agapitov, and V. V. Krasnoselskikh (2013), Para-  
 571 metric validations of analytical lifetime estimates for radiation belt electron diffusion  
 572 by whistler waves, *Annales Geophysicae*, 31, 599–624, doi:10.5194/angeo-31-599-2013.

573 Cao, J., et al. (2008), Characteristics of middle- to low-latitude pi2 excited by bursty bulk  
 574 flows, *Journal of Geophysical Research Atmospheres*, 113(A7), 521–532.

575 Cao, J. B., W. Z. Ding, H. Reme, I. Dandouras, M. Dunlop, Z. X. Liu, and J. Y. Yang  
 576 (2011), The statistical studies of the inner boundary of plasma sheet, *Annales Geophys-  
 577 icae*, 29(2), 289–298, doi:10.5194/angeo-29-289-2011.

578 Cao, J. B., et al. (2010), Geomagnetic signatures of current wedge produced by fast flows  
579 in a plasma sheet, *Journal of Geophysical Research Atmospheres*, 115(A8).

580 Chappell, C. R., K. K. Harris, and G. W. Sharp (1970), The morphology of the bulge re-  
581 gion of the plasmasphere, *Journal of Geophysical Research Atmospheres*, 75(75), 3848–  
582 3861.

583 Chen, M. W., C. L. Lemon, T. B. Guild, A. M. Keesee, A. Lui, J. Goldstein, J. V.  
584 Rodriguez, and P. C. Anderson (2015a), Effects of modeled ionospheric conductance  
585 and electron loss on self-consistent ring current simulations during the 57 april 2010  
586 storm, *Journal of Geophysical Research: Space Physics*, 120(7), 5355–5376, doi:  
587 10.1002/2015JA021285, 2015JA021285.

588 Chen, M. W., C. L. Lemon, K. Orlova, Y. Shprits, J. Hecht, and R. L. Walterscheid  
589 (2015b), Comparison of simulated and observed trapped and precipitating electron  
590 fluxes during a magnetic storm, *Geophysical Research Letters*, 42(20), 8302–8311, doi:  
591 10.1002/2015GL065737, 2015GL065737.

592 Daglis, I., and J. Kozyra (2002), Outstanding issues of ring current dynamics,  
593 *Journal of Atmospheric and Solar-Terrestrial Physics*, 64(2), 253 – 264, doi:  
594 [http://dx.doi.org/10.1016/S1364-6826\(01\)00087-6](http://dx.doi.org/10.1016/S1364-6826(01)00087-6), sTEP-Results, Applications and  
595 Modelling Phase (S-RAMP).

596 Daglis, I. A., R. M. Thorne, B. Wolfgang, and O. Stefano (1999), The terrestrial ring  
597 current: Origin, formation, and decay, *Reviews of Geophysics*, 37(4), 407–438.

598 De Zeeuw, D. L., S. Sazykin, R. A. Wolf, T. I. Gombosi, A. J. Ridley, and G. Tóth  
599 (2004), Coupling of a global MHD code and an inner magnetospheric model: Ini-  
600 tial results, *Journal of Geophysical Research (Space Physics)*, 109, A12219, doi:

601 10.1029/2003JA010366.

602 Dessler, A. J., and E. N. Parker (1959), Hydromagnetic Theory of Geomagnetic Storms,  
603 *J. Geophys. Res.*, 64, 2239–2252, doi:10.1029/JZ064i012p02239.

604 Ebihara, Y., M.-C. Fok, R. A. Wolf, T. J. Immel, and T. E. Moore (2004), Influence of  
605 ionosphere conductivity on the ring current, *Journal of Geophysical Research (Space*  
606 *Physics)*, 109, A08205, doi:10.1029/2003JA010351.

607 Ebihara, Y., N. Nishitani, T. Kikuchi, T. Ogawa, K. Hosokawa, M.-C. Fok, and M. F.  
608 Thomsen (2009), Dynamical property of storm time subauroral rapid flows as a man-  
609 ifestation of complex structures of the plasma pressure in the inner magnetosphere,  
610 *Journal of Geophysical Research: Space Physics*, 114 (A1), doi:10.1029/2008JA013614.

611 Fok, M.-C., R. A. Wolf, R. W. Spiro, and T. E. Moore (2001), Comprehensive computa-  
612 tional model of Earth's ring current, *jgr*, 106, 8417–8424, doi:10.1029/2000JA000235.

613 Foster, J. C., and W. J. Burke (2002), Saps: A new categorization for sub-auroral  
614 electric fields, *Eos, Transactions American Geophysical Union*, 83(36), 393–394, doi:  
615 10.1029/2002EO000289.

616 Galand, M., and A. D. Richmond (2001), Ionospheric electrical conductances produced by  
617 auroral proton precipitation, *Journal of Geophysical Research: Space Physics*, 106(A1),  
618 117–125, doi:10.1029/1999JA002001.

619 Gkioulidou, M., C.-P. Wang, L. R. Lyons, and R. A. Wolf (2009), Formation of the  
620 harang reversal and its dependence on plasma sheet conditions: Rice convection model  
621 simulations, *Journal of Geophysical Research: Space Physics*, 114 (A7), n/a–n/a, doi:  
622 10.1029/2008JA013955, a07204.

623 Glauert, S. A., and R. B. Horne (2005), Calculation of pitch angle and energy diffusion  
 624 coefficients with the PADIE code, *Journal of Geophysical Research (Space Physics)*,  
 625 110, A04206, doi:10.1029/2004JA010851.

626 Glauert, S. A., R. B. Horne, and N. P. Meredith (2014), Three-dimensional electron  
 627 radiation belt simulations using the BAS Radiation Belt Model with new diffusion  
 628 models for chorus, plasmaspheric hiss, and lightning-generated whistlers, *Journal of*  
 629 *Geophysical Research (Space Physics)*, 119, 268–289, doi:10.1002/2013JA019281.

630 Harang, L. (1946), The mean field of disturbance of polar geomagnetic storms, *Terrestrial*  
 631 *Magnetism and Atmospheric Electricity*, 51(3), 353380.

632 Hardy, D. A., M. S. Gussenhoven, R. Raistrick, and W. J. Mcneil (1987), Statistical  
 633 and functional representations of the pattern of auroral energy flux, number flux, and  
 634 conductivity, *Journal of Geophysical Research Atmospheres*, 92(A11), 12,275–12,294.

635 Horne, R. B., R. M. Thorne, N. P. Meredith, and R. R. Anderson (2003), Diffuse auroral  
 636 electron scattering by electron cyclotron harmonic and whistler mode waves during  
 637 an isolated substorm, *Journal of Geophysical Research: Space Physics*, 108(A7), doi:  
 638 10.1029/2002JA009736, 1290.

639 Horne, R. B., T. Kersten, S. A. Glauert, N. P. Meredith, D. Boscher, A. Sicard-Piet, R. M.  
 640 Thorne, and W. Li (2013), A new diffusion matrix for whistler mode chorus waves, *Jour-*  
 641 *nal of Geophysical Research (Space Physics)*, 118, 6302–6318, doi:10.1002/jgra.50594.

642 Horwitz, J. L. (1987), Core plasma in the magnetosphere, *Reviews of Geophysics*, 25(3),  
 643 579–587, doi:10.1029/RG025i003p00579.

644 Huba, J. D., and S. Sazykin (2014), Storm time ionosphere and plasmasphere structuring:  
 645 Sami3-rcm simulation of the 31 march 2001 geomagnetic storm, *Geophysical Research*

646 *Letters*, 41(23), 8208–8214, doi:10.1002/2014GL062110, 2014GL062110.

647 Huba, J. D., S. Sazykin, and A. Coster (2017), Sami3-rcm simulation of the 17 march 2015  
648 geomagnetic storm, *Journal of Geophysical Research: Space Physics*, 122(1), 1246–1257,  
649 doi:10.1002/2016JA023341, 2016JA023341.

650 Ilie, R., M. W. Liemohn, G. Toth, and R. M. Skoug (2012), Kinetic model of the inner  
651 magnetosphere with arbitrary magnetic field, *Journal of Geophysical Research: Space  
652 Physics*, 117(A4), n/a–n/a, doi:10.1029/2011JA017189, a04208.

653 Jordanova, V. K., Y. S. Miyoshi, S. Zaharia, M. F. Thomsen, G. D. Reeves, D. S. Evans,  
654 C. G. Mouikis, and J. F. Fennell (2006), Kinetic simulations of ring current evolution  
655 during the Geospace Environment Modeling challenge events, *Journal of Geophysical  
656 Research (Space Physics)*, 111, A11S10, doi:10.1029/2006JA011644.

657 Jordanova, V. K., S. Zaharia, and D. T. Welling (2010), Comparative study of ring current  
658 development using empirical, dipolar, and self-consistent magnetic field simulations, *jgr*,  
659 115, A00J11, doi:10.1029/2010JA015671.

660 Jordanova, V. K., D. T. Welling, S. G. Zaharia, L. Chen, and R. M. Thorne (2012),  
661 Modeling ring current ion and electron dynamics and plasma instabilities during a  
662 high-speed stream driven storm, *jgr*, 117(A9), doi:10.1029/2011JA017433.

663 Kelley, M. C., and R. A. Heelis (1989), The earth's ionosphere [electronic resource] :  
664 plasma physics and electrodynamics /.

665 Khazanov, G. V., M. W. Liemohn, T. S. Newman, M.-C. Fok, and R. W. Spiro (2003),  
666 Self-consistent magnetosphere-ionosphere coupling: Theoretical studies, *Journal of Geo-  
667 physical Research (Space Physics)*, 108, 1122, doi:10.1029/2002JA009624.

668 Li, L. Y., J. Yu, J. B. Cao, D. Zhang, X. H. Wei, Z. J. Rong, J. Y. Yang, and H. S. Fu  
669 (2013), Rapid loss of the plasma sheet energetic electrons associated with the growth  
670 of whistler mode waves inside the bursty bulk flows, *Journal of Geophysical Research:*  
671 *Space Physics*, 118(11), 7200–7210, doi:10.1002/2013JA019109, 2013JA019109.

672 Liemohn, M. W., A. J. Ridley, D. L. Gallagher, D. M. Ober, and J. U. Kozyra (2004),  
673 Dependence of plasmaspheric morphology on the electric field description during the  
674 recovery phase of the 17 april 2002 magnetic storm, *Journal of Geophysical Research:*  
675 *Space Physics*, 109(A3), n/a–n/a, doi:10.1029/2003JA010304, a03209.

676 Liemohn, M. W., A. J. Ridley, P. C. Brandt, D. L. Gallagher, J. U. Kozyra, D. M.  
677 Ober, D. G. Mitchell, E. C. Roelof, and R. DeMajistre (2005), Parametric analysis  
678 of nightside conductance effects on inner magnetospheric dynamics for the 17 april  
679 2002 storm, *Journal of Geophysical Research: Space Physics*, 110(A12), n/a–n/a, doi:  
680 10.1029/2005JA011109, a12S22.

681 Liu, X., W. Liu, J. B. Cao, H. S. Fu, J. Yu, and X. Li (2015), Dynamic plasmapause  
682 model based on themis measurements, *Journal of Geophysical Research: Space Physics*,  
683 120(12), 10,543–10,556, doi:10.1002/2015JA021801, 2015JA021801.

684 Matsui, H., V. K. Jordanova, J. M. Quinn, R. B. Torbert, and G. Paschmann (2004),  
685 Derivation of electric potential patterns in the inner magnetosphere from cluster edi  
686 data: Initial results, *Journal of Geophysical Research Atmospheres*, 109(A10), A10,202.

687 Matsui, H., R. B. Torbert, H. E. Spence, Y. V. Khotyaintsev, and P. . Lindqvist (2013),  
688 Revision of empirical electric field modeling in the inner magnetosphere using cluster  
689 data, *Journal of Geophysical Research Space Physics*, 118(7), 4119–4134.

690 Moen, J., and A. Brekke (1993), The solar flux influence on quiet time conductances in  
691 the auroral ionosphere, *grl*, 20, 971–974, doi:10.1029/92GL02109.

692 Newell, P. T., T. Sotirelis, and S. Wing (2009), Diffuse, monoenergetic, and broadband au-  
693 rora: The global precipitation budget, *Journal of Geophysical Research: Space Physics*,  
694 114(A9), n/a–n/a, doi:10.1029/2009JA014326, a09207.

695 Ni, B., R. M. Thorne, Y. Y. Shprits, and J. Bortnik (2008), Resonant scattering of plasma  
696 sheet electrons by whistler-mode chorus: Contribution to diffuse auroral precipitation,  
697 *Geophysical Research Letters*, 35(11), n/a–n/a, doi:10.1029/2008GL034032, 111106.

698 Nishimura, Y., A. Shinbori, T. Ono, M. Iizima, and A. Kumamoto (2006), Stormtime  
699 electric field distribution in the inner magnetosphere, *Geophysical Research Letters*,  
700 33(22), 121–132.

701 Nishimura, Y., A. Shinbori, T. Ono, M. Iizima, and A. Kumamoto (2007), Evolution  
702 of ring current and radiation belt particles under the influence of storm-time elec-  
703 tric fields, *Journal of Geophysical Research: Space Physics*, 112(A6), n/a–n/a, doi:  
704 10.1029/2006JA012177, a06241.

705 Richmond, A. D., and Y. Kamide (1988), Mapping electrodynamic features of the high-  
706 latitude ionosphere from localized observations: Technique, *Journal of Geophysical Re-  
707 search: Space Physics*, 93(A6), 5741–5759, doi:10.1029/JA093iA06p05741.

708 Ridley, A., T. Gombosi, and D. Dezeeuw (2004), Ionospheric control of the magnetosphere:  
709 conductance, *Annales Geophysicae*, 22, 567–584, doi:10.5194/angeo-22-567-2004.

710 Ridley, A. J., and M. W. Liemohn (2002), A model-derived storm time asymmetric  
711 ring current driven electric field description, *Journal of Geophysical Research (Space  
712 Physics)*, 107, 1151, doi:10.1029/2001JA000051.

713 Robinson, R. M., R. R. Vondrak, K. Miller, T. Dabbs, and D. Hardy (1987), On calculating  
714 ionospheric conductances from the flux and energy of precipitating electrons, *jgr*, 92,  
715 2565–2569, doi:10.1029/JA092iA03p02565.

716 Rowland, D. E., and J. R. Wygant (1998), Dependence of the large-scale, inner magne-  
717 toospheric electric field on geomagnetic activity, *Journal of Geophysical Research: Space*  
718 *Physics*, 103(A7), 14,959–14,964, doi:10.1029/97JA03524.

719 Sckopke, N. (1966), A General Relation between the Energ of Trapped Particles  
720 and the Disturbance Field near the Earth, *J. Geophys. Res.*, 71, 3125–3130, doi:  
721 10.1029/JZ071i013p03125.

722 Stern, D. P. (1975), The motion of a proton in the equatorial magnetosphere, *Journal of*  
723 *Geophysical Research (Space Physics)*, 80, 595–599, doi:10.1029/JA080i004p00595.

724 Toffoletto, F., S. Sazykin, R. Spiro, and R. Wolf (2003), Inner magnetospheric  
725 modeling with the Rice Convection Model, *Space Sci. Rev.*, 107, 175–196, doi:  
726 10.1023/A:1025532008047.

727 Tsyganenko, N. A. (1989), A magnetospheric magnetic field model with a warped tail  
728 current sheet, *Planet. Space Sci.*, 37, 5–20, doi:10.1016/0032-0633(89)90066-4.

729 Vasyliunas, V. M. (1970), Mathematical Models of Magnetospheric Convection and Its  
730 Coupling to the Ionosphere, in *Particles and Field in the Magnetosphere, Astrophysics*  
731 and *Space Science Library*, vol. 17, edited by B. M. McCormack and A. Renzini, p. 60.

732 Volland, H. (1973), A Semiempirical Model of Large-Scale Magnetospheric Elec-  
733 tric Fields, *Journal of Geophysical Research (Space Physics)*, 78, 171–180, doi:  
734 10.1029/JA078i001p00171.

735 Wang, H., H. Lühr, A. Ridley, and T. Huang (2014), The spatial distribution of region 2  
736 field-aligned currents relative to subauroral polarization stream, *Annales Geophysicae*,  
737 32(5), 533–542, doi:10.5194/angeo-32-533-2014.

738 Weimer, D. R. (2001), An improved model of ionospheric electric potentials including sub-  
739 storm perturbations and application to the Geospace Environment Modeling November  
740 24, 1996, event, *Journal of Geophysical Research (Space Physics)*, 106, 407–416, doi:  
741 10.1029/2000JA000604.

742 Weimer, D. R. (2005), Improved ionospheric electrodynamic models and application to cal-  
743 culating joule heating rates, *Journal of Geophysical Research: Space Physics*, 110(A5),  
744 n/a–n/a, doi:10.1029/2004JA010884, a05306.

745 Young, D. T., H. Balsiger, and J. Geiss (1982), Correlations of magnetospheric ion com-  
746 position with geomagnetic and solar activity, *Journal of Geophysical Research: Space  
747 Physics*, 87(A11), 9077–9096, doi:10.1029/JA087iA11p09077.

748 Yu, Y., V. Jordanova, S. Zou, R. Heelis, M. Ruohoniemi, and J. Wygant (2015), Mod-  
749 eling subauroral polarization streams during the 17 march 2013 storm, *Journal of  
750 Geophysical Research: Space Physics*, 120(3), 1738–1750, doi:10.1002/2014JA020371,  
751 2014JA020371.

752 Yu, Y., V. K. Jordanova, A. J. Ridley, J. M. Albert, R. B. Horne, and C. A. Jeffery  
753 (2016), A new ionospheric electron precipitation module coupled with ram-scb within  
754 the geospace general circulation model, *Journal of Geophysical Research: Space Physics*,  
755 121(9), 8554–8575, doi:10.1002/2016JA022585, 2016JA022585.

756 Zaharia, S., C. Cheng, and K. Maezawa (2004), 3-D force-balanced magnetospheric con-  
757 figurations, *Annales Geophysicae*, 22, 251–265, doi:10.5194/angeo-22-251-2004.

758 Zaharia, S., V. K. Jordanova, M. F. Thomsen, and G. D. Reeves (2006), Self-consistent  
759 modeling of magnetic fields and plasmas in the inner magnetosphere: Application to a  
760 geomagnetic storm, *jgr*, 111, A11S14, doi:10.1029/2006JA011619.

761 Zaharia, S., V. K. Jordanova, D. Welling, and G. Tóth (2010), Self-consistent inner  
762 magnetosphere simulation driven by a global MHD model, *jgr*, 115, A12,228, doi:  
763 10.1029/2010JA015915.

764 Zhang, D., J. B. Cao, X. H. Wei, and L. Y. Li (2015), New technique to calculate electron  
765 alfvén layer and its application in interpreting geosynchronous access of ps energetic  
766 electrons, *Journal of Geophysical Research Space Physics*, 7(1), 1–18.

767 Zou, S., L. R. Lyons, C.-P. Wang, A. Boudouridis, J. M. Ruohoniemi, P. C. Anderson,  
768 P. L. Dyson, and J. C. Devlin (2009), On the coupling between the harang reversal  
769 evolution and substorm dynamics: A synthesis of superdarn, dmsp, and image ob-  
770 servations, *Journal of Geophysical Research: Space Physics*, 114(A1), n/a–n/a, doi:  
771 10.1029/2008JA013449, a01205.

**Figure 1.** The coupling within the RAM-SCB-E model. The part within the dashed box is used to implement the self-consistency of electric field using inputs of  $J_{||}$  and precipitation energy flux  $F_E$  from the kinetic ring current model.

**Figure 2.** Solar wind and interplanetary magentic field conditions and geomagnetic AL and SYM-H index during the storm event occurred on August 31, 2005.

**Figure 3.** Particle flux obtained from LANL-GEO satellites (e.g., LANL-1989, LANL-1990, LANL-1994, LANL-1997, LANL-2001) were available during the storm event in this study) is used to specify the boundary condition for the model at  $L = 6.5$ . The electron and proton fluxes at  $MLT=0$  are selected for demonstration.

**Figure 4.** Magnetic equatorial potential pattern (top) and the Y component of the convection electric field (bottom) in the self-consistent electric field method (left) and Weimer potential model (right). The dashed circles in each plot indicates  $L$  shells at 2, 4, and 6 respectively.

**Figure 5.** Dawn-to-dusk convection electric field component at  $MLT = 20$  in the self-consistent electric field approach (left) and Weimer model (right). Top row shows electric field as a function of  $L$  and UT, and bottom row shows electric field as function of  $L$  at four selected times, covering from pre-storm, storm main phase, and recovery phase.

**Figure 6.** Ring current proton and electron flux as function of  $L$  shell and time selected at  $MLT = 20$  for protons and  $MLT = 4$  for electrons. (a, c) use self-consistent electric field model. (b, d) use Weimer electric potential model. During the storm main phase, low energy protons are convected towards the Earth with the aid of convection electric field. The Weimer potential model shows more profound effect on the low-energy plasma transport as they penetrate well deep down to  $2.0 R_e$ , but they are nearly prohibited at  $2.5 R_e$  when a self-consistent electric field model is used. For high-energy protons and electrons in various energy, their inward transport is similar in both simulations.

**Figure 7.** Ring current proton flux at 9.3 keV (top row) and 100 keV (bottom row) with pitch angle near 90°. In the case with self-consistent electric field, low-energy protons are convected from dusk to dawn through midnight, affected by the potential contours that are skewed towards early morning sector as shown in Figure 4. On the contrary, under the prescribed Weimer potential, low-energy protons preferentially convect towards dayside mainly through the dusk side. The high-energy proton fluxes are similar in both cases.

**Figure 8.** Global pattern of (a) ionospheric FACs, (b) Pedersen conductance, (c, e) electric potential, and (d, f) eastward flow in the ionosphere altitude from simulations with either both self-consistent (top two rows) or Weimer (bottom row) electric field.

**Figure 9.** Simulation results from using self-consistent electric field: latitudinal distribution of FACs, Pedersen and Hall conductance, precipitated electron energy flux, poleward electric field, and eastward drift velocity at the ionospheric altitude for MLT = 21. The vertical dashed line denotes the equatorward boundary of auroral precipitation, where precipitation is significantly lower in the subauroral region than in the auroral latitudes.

**Figure 10.** Comparisons of flow speed and Pedersen conductance between the self-consistent simulation (blue) and DMSP measurements (black). All passes are in the northern hemisphere, flying from the dusk side to dawn side. Negative cross-track flow represents a westward velocity to the left of the trajectory direction. The Pedersen conductance based on observations is calculated from the measured precipitation flux (here, the solid black line marks the conductance associated with both electron and ion precipitation, and dashed black line denotes that only from electron precipitation).

**Figure 11.** Measured SYM-H index (black) and simulated Dst index using different electric field models. “IESC” stands for self-consistent electric field, “VOLS” is for Volland-Stern electric field, and “Weimer” uses Weimer potential model.

**Figure 1.**

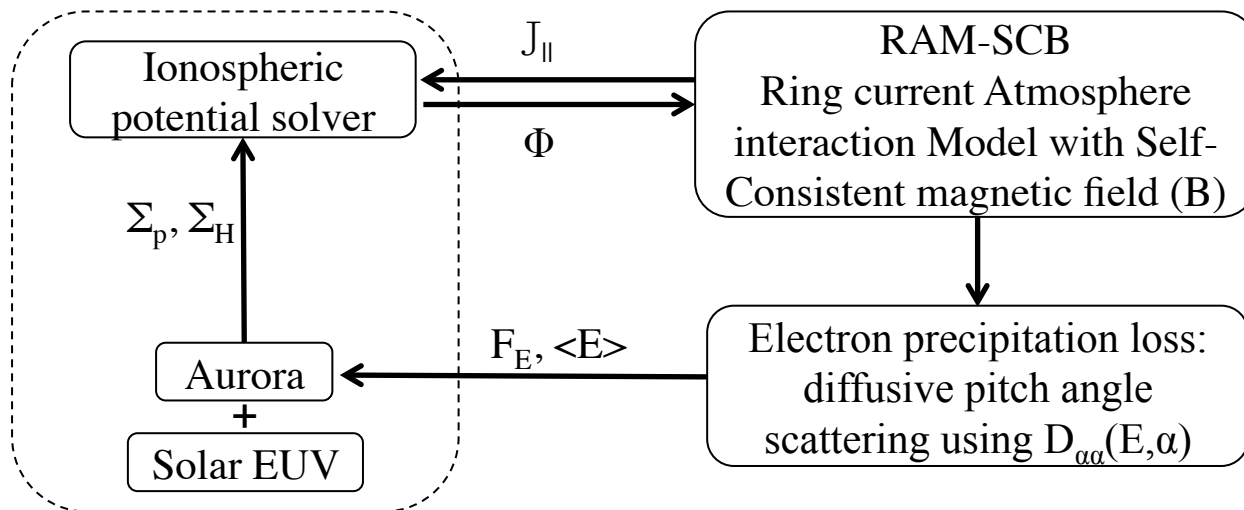


**Figure 2.**

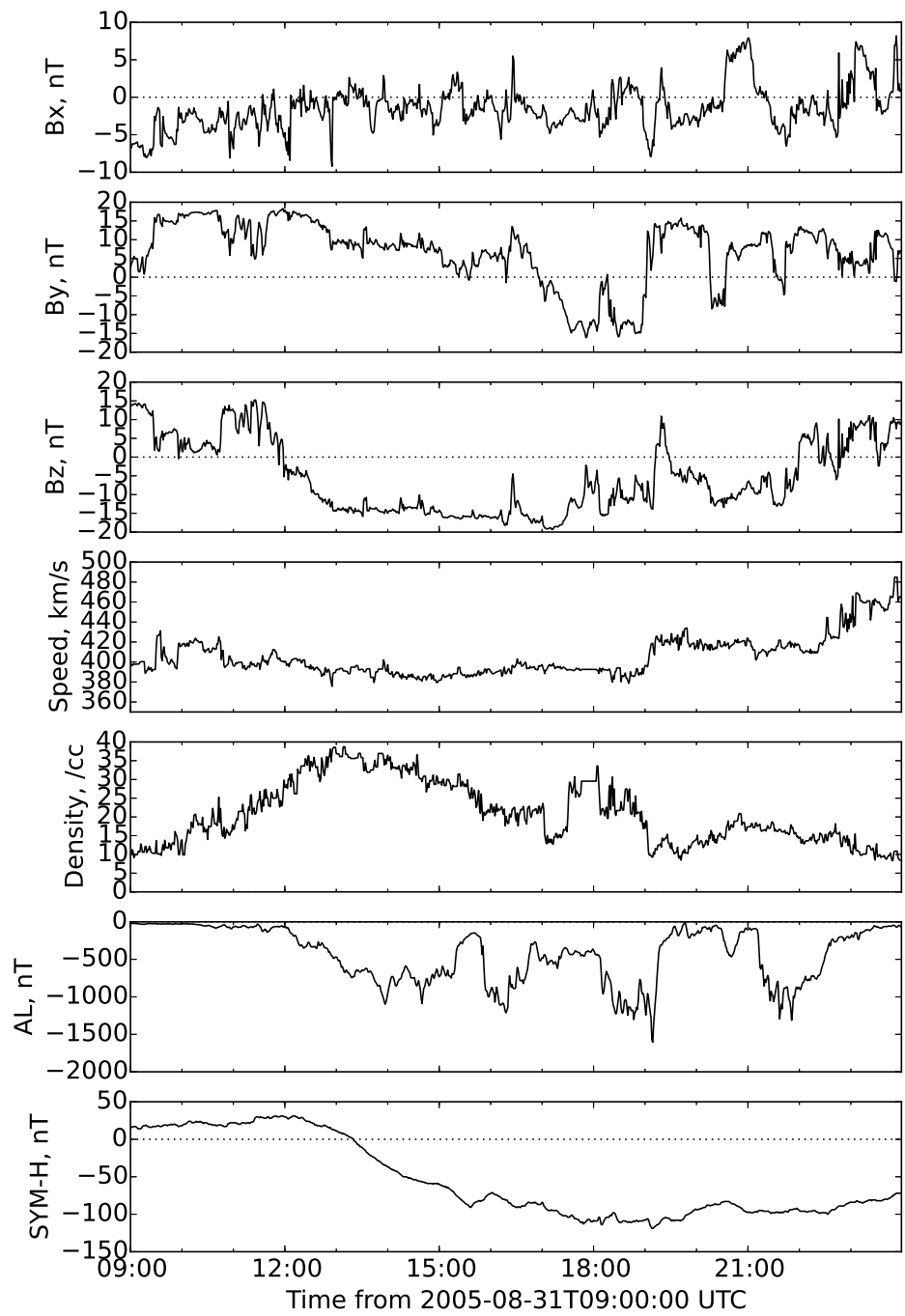


**Figure 3.**

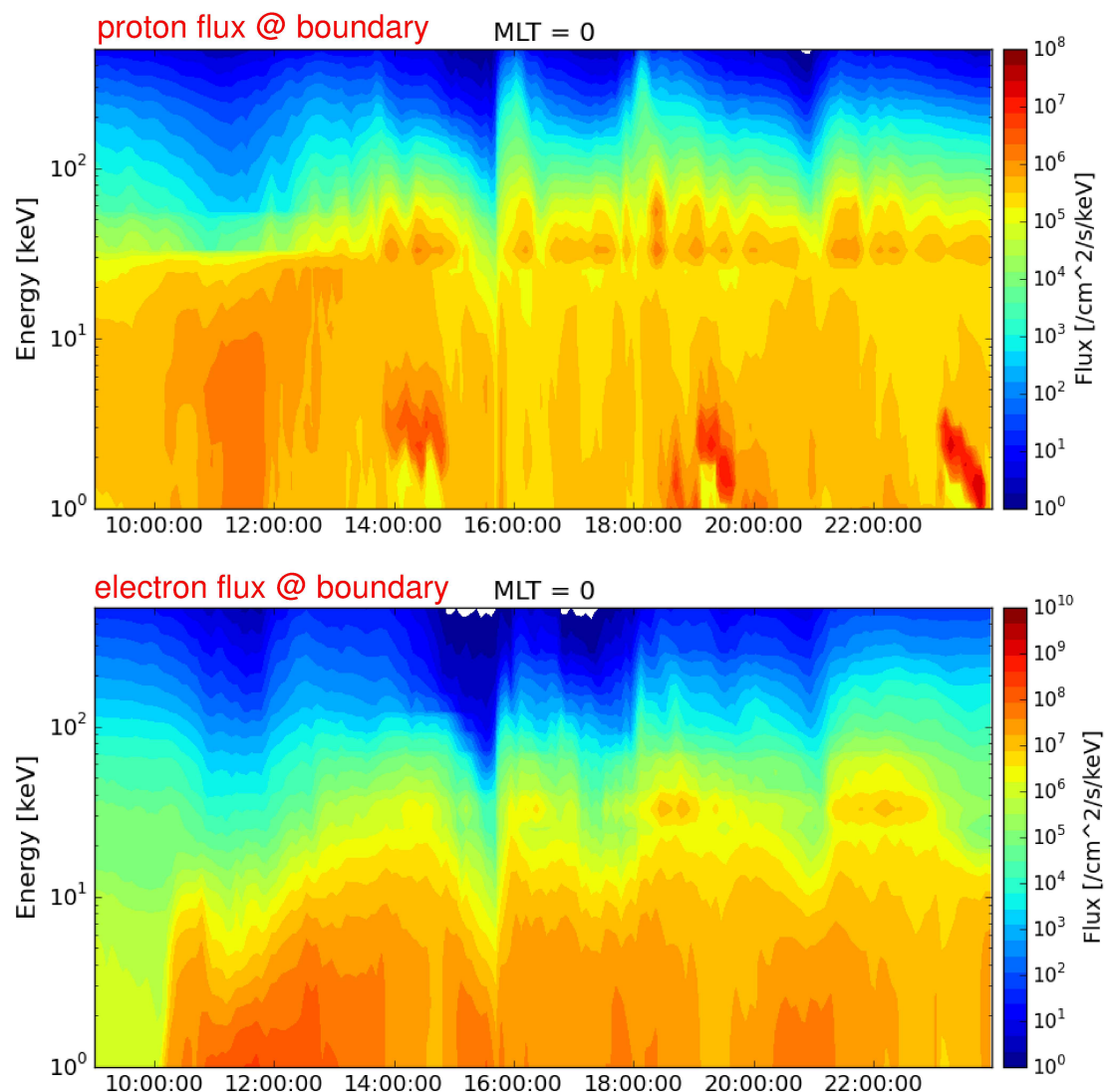


**Figure 4.**

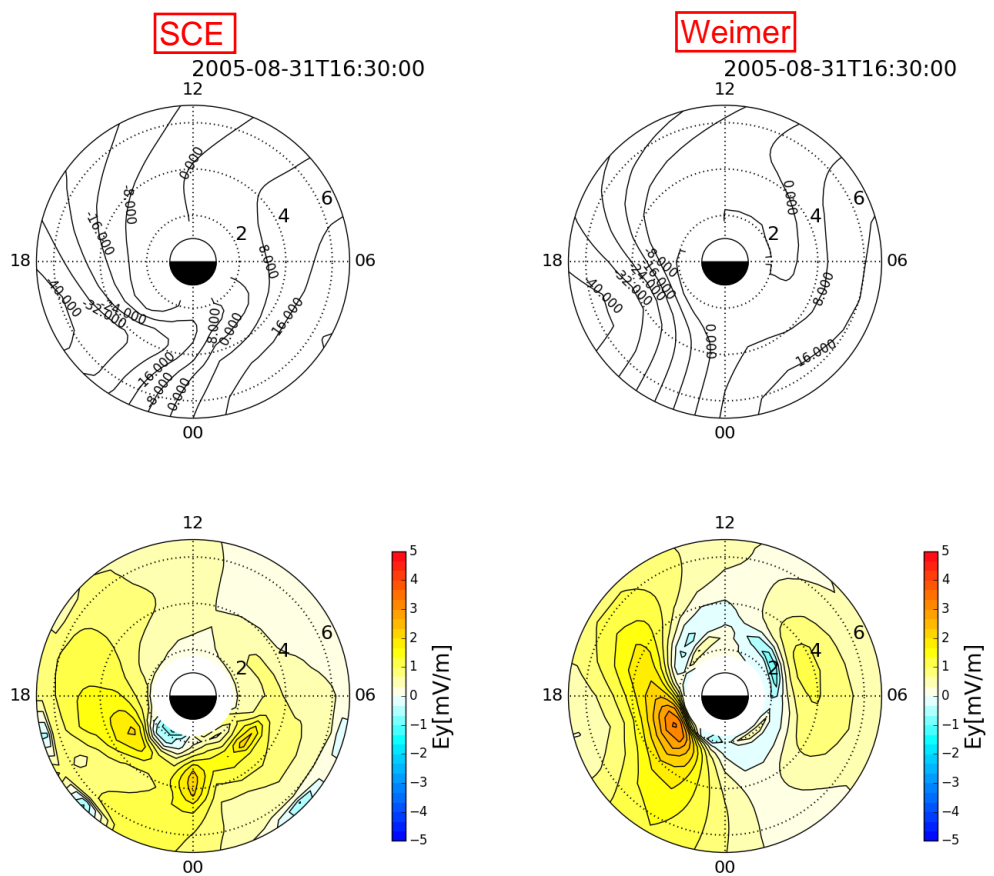


**Figure 5.**

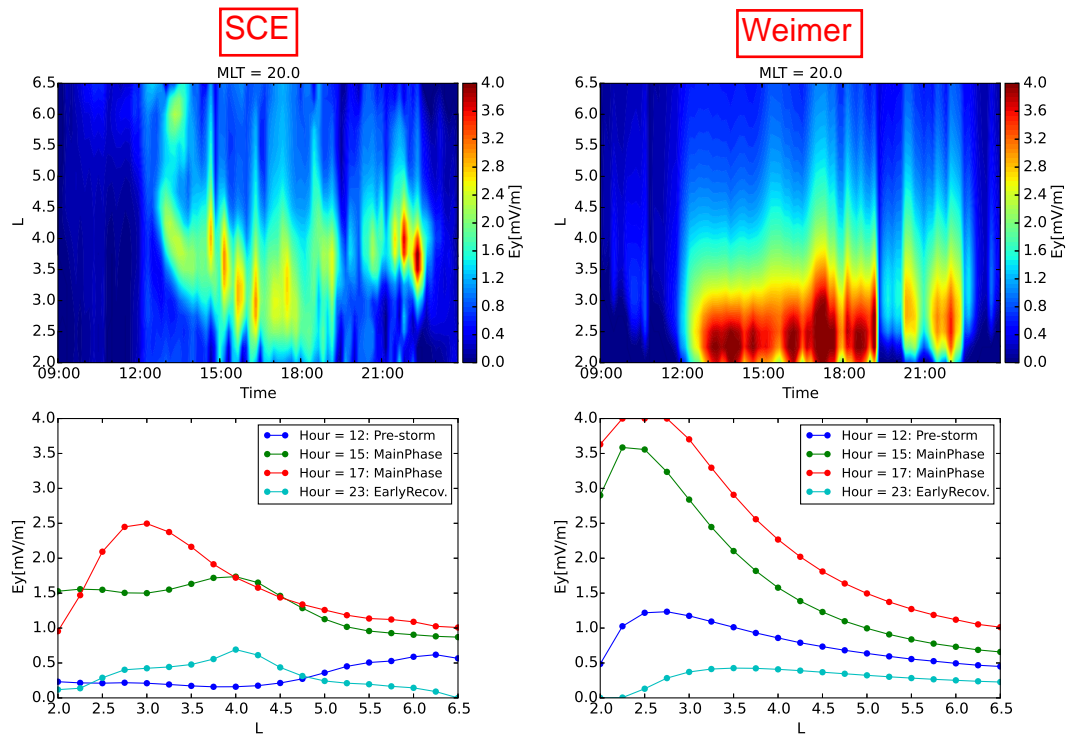


**Figure 6.**

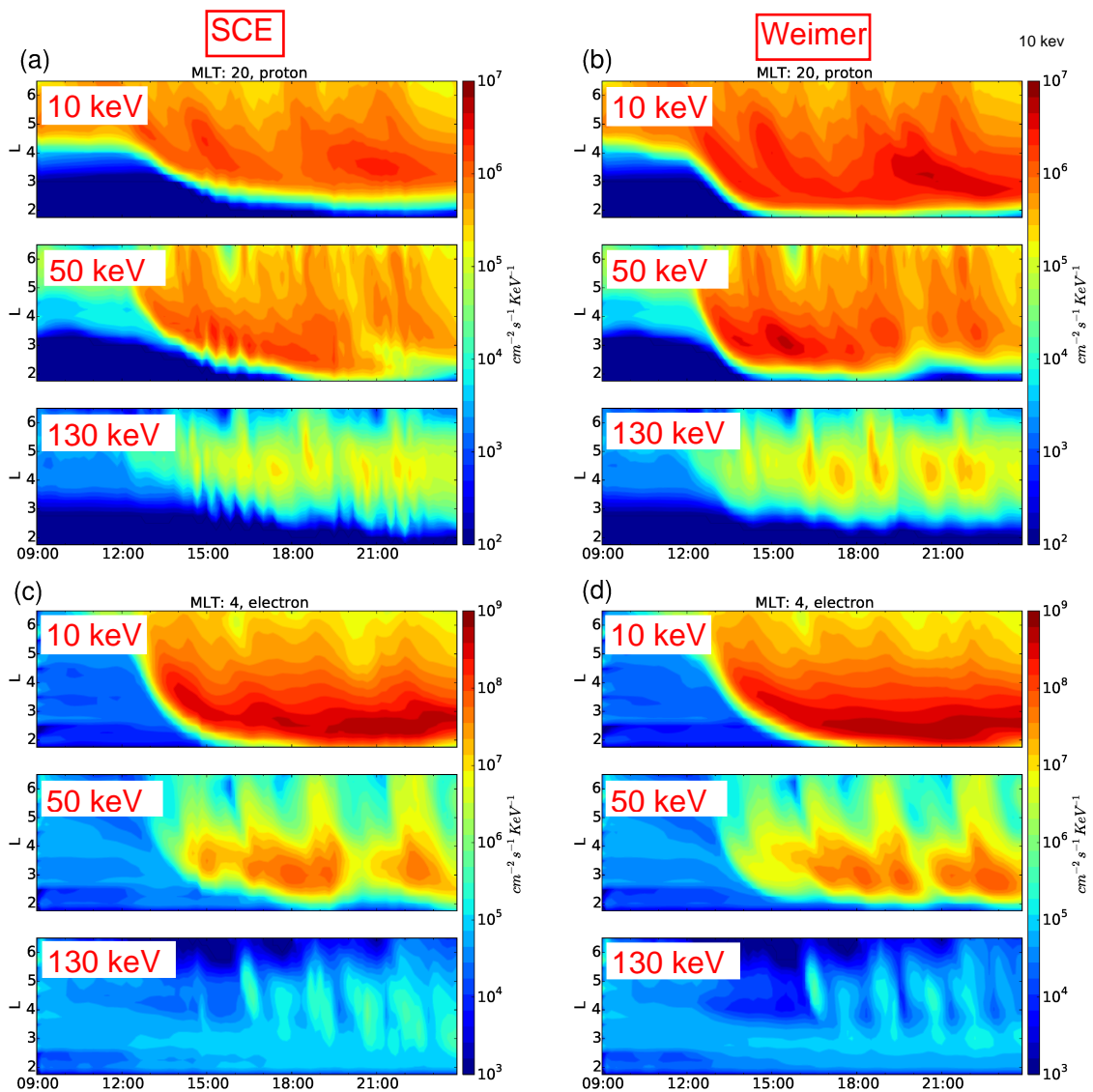


**Figure 7.**

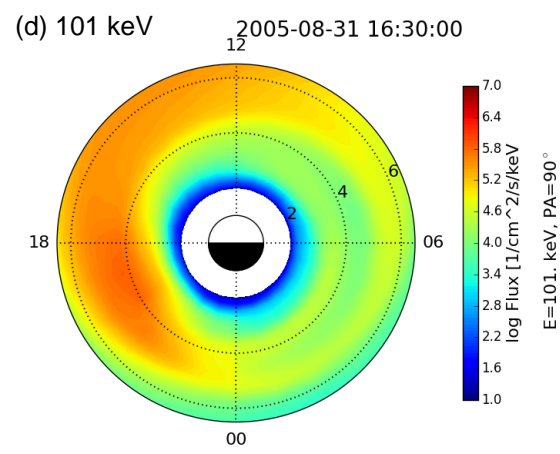
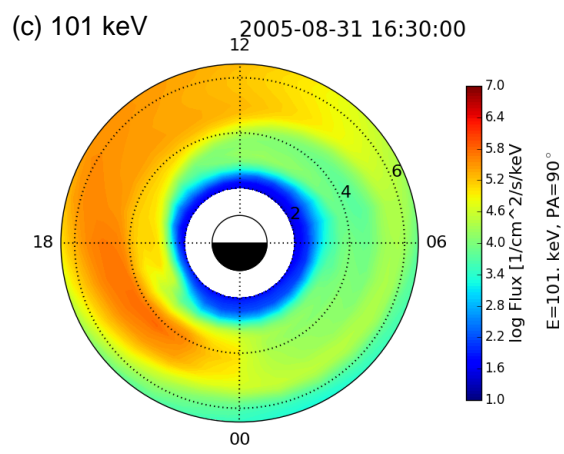
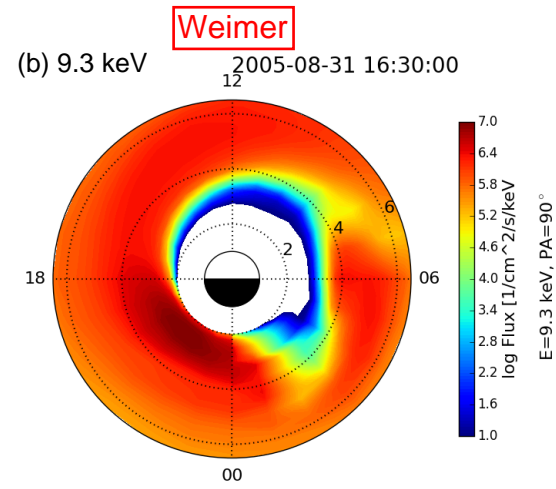
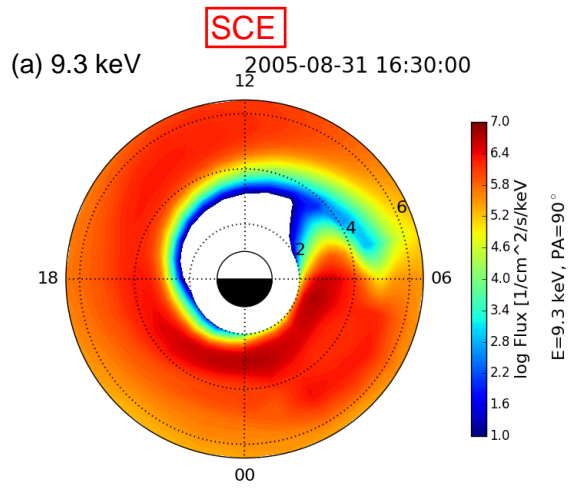


**Figure 8.**

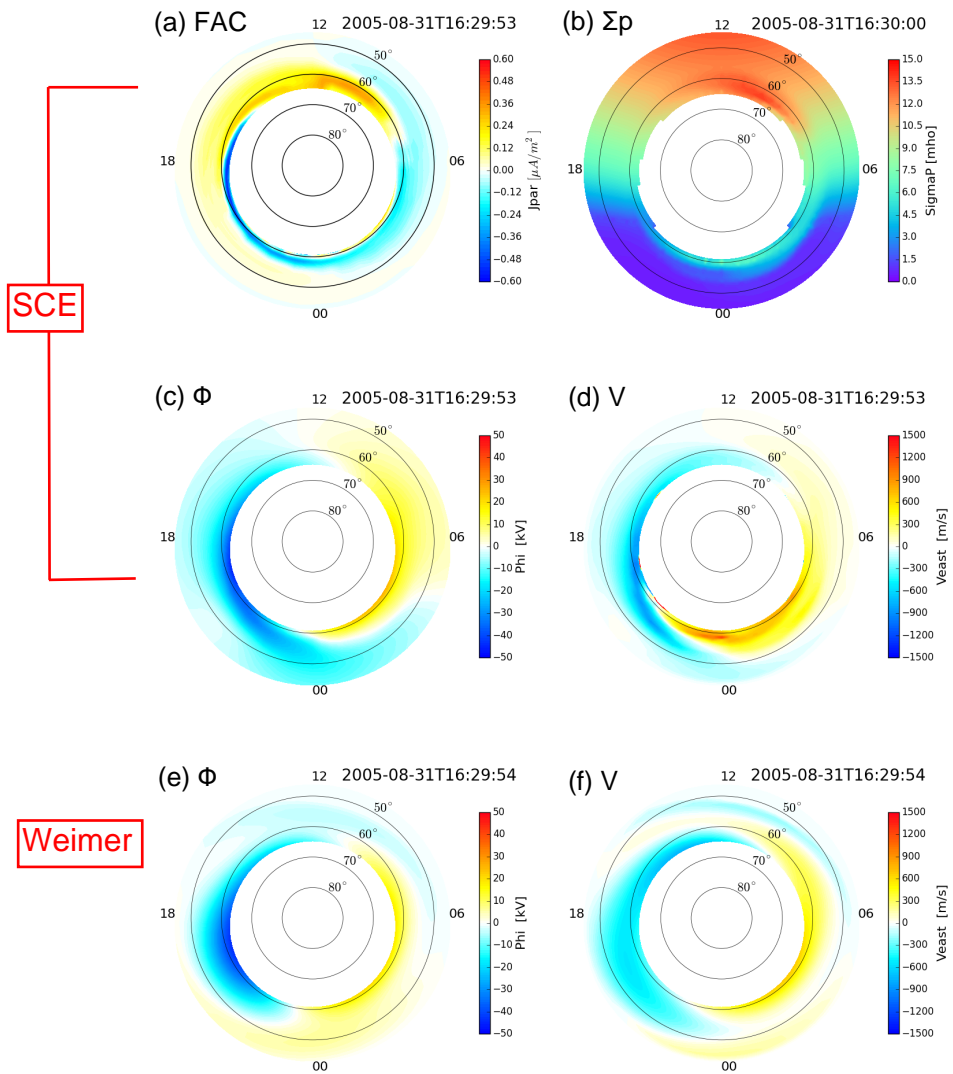


**Figure 9.**

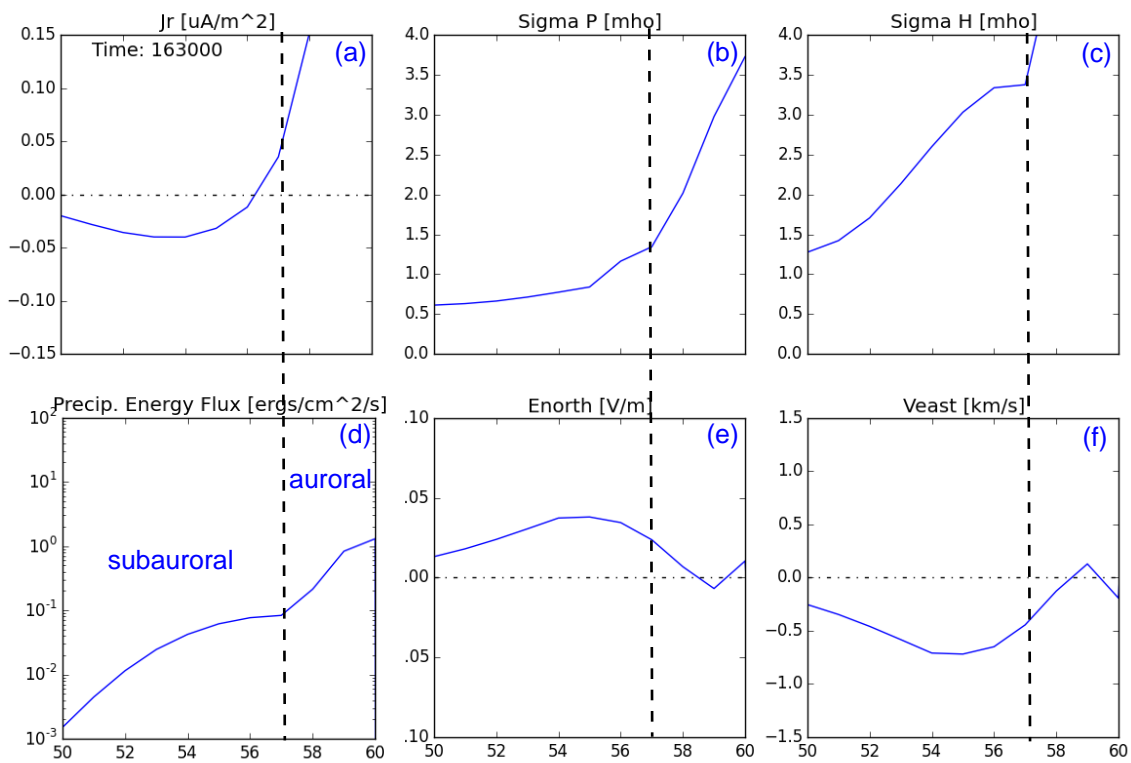


**Figure 10.**

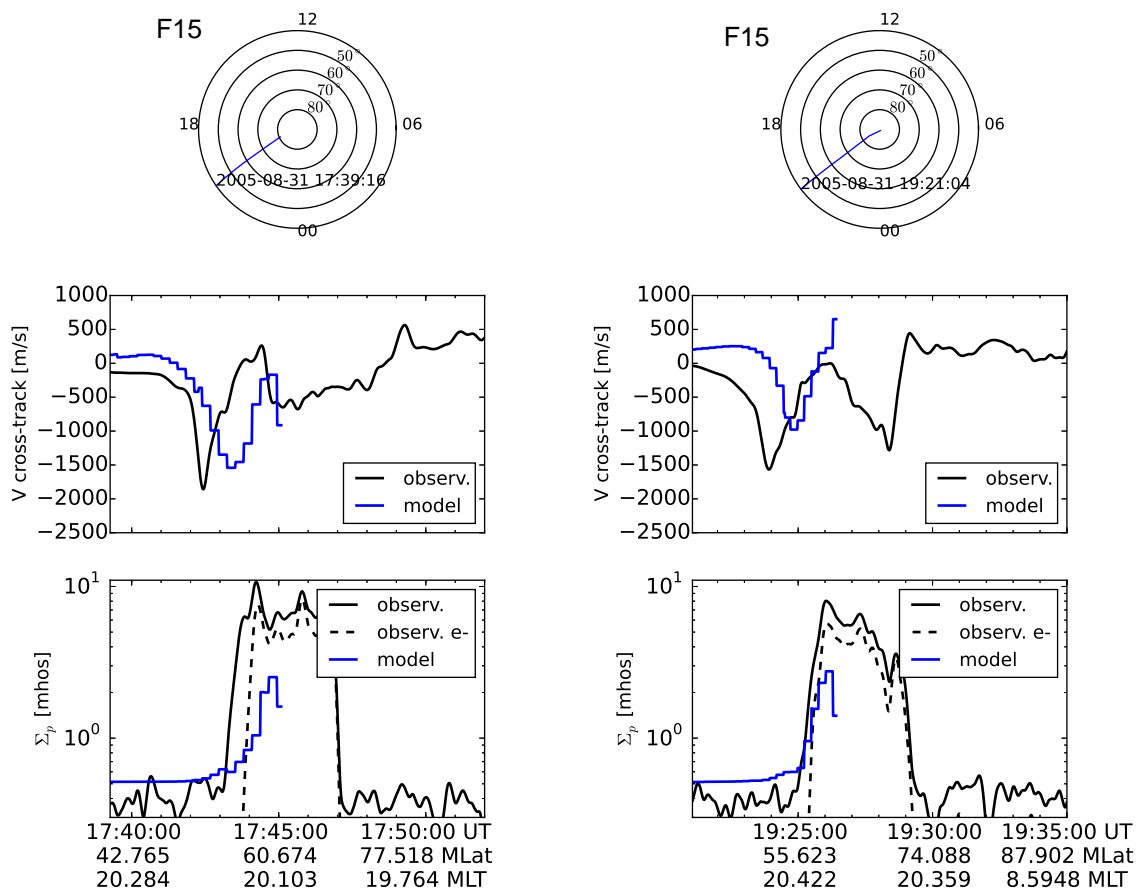


**Figure 11.**

